

Article

# Printable and Flexible Iridium Oxide-Based pH Sensor by a Roll-to-Roll Process

Khengdauliu Chawang , Sen Bing  and Jung-Chih Chiao \* 

Electrical and Computer Engineering, Southern Methodist University, Dallas, TX 75205, USA

\* Correspondence: jchiao@smu.edu

**Abstract:** A flexible pH sensor based on using iridium oxide ( $\text{IrO}_x$ ) as the sensing film was developed by the roll-to-roll (R2R) process. The inert and biocompatible properties of  $\text{IrO}_x$  make it a desired metal oxide for pH-sensing applications. The flexible substrates being continuously processed by the R2R technique provides the advantages of scalability, reconfigurability, resiliency, on-demand manufacturing, and high throughput, without the need for vacuum systems. Potential sweeps by cyclic voltammetry across the  $\text{IrO}_x$  film against commercial and planar Ag/AgCl electrodes validated the reversible electrochemical mechanisms. Multiple  $\text{IrO}_x$  electrodes showed similar output potentials when continuously tested in the pH range of 2–13, indicating good fabrication uniformity. For practical applications, planar  $\text{IrO}_x/\text{Ag-AgCl}$  pairs developed on polyimide substrates were tested, with a good linear fit within pH 2–13, achieving Nernstian responses of around  $-60.6$  mV/pH. The pH sensors showed good repeatability when analyzed with hysteresis, drift, fluctuation, and deviation as the stability factors. The selectivity of the interference ions and the effect of temperature were studied and compared with the reported values. The electrodes were further laminated in a process compatible with the R2R technique for packaging. The flexible sensors were tested under flat and curved surface conditions. Tests in artificial sweat and viscous solutions were analyzed in the Clarke error grid, showing reliable pH-sensing performance. The materials used during the manufacturing processes were sustainable, as the active materials were in small amounts and there was no waste during processing. No toxic chemicals were needed in the fabrication processes. The cost-effective and efficient materials and the fabrication process allow for rapid production that is necessary for disposable and point-of-care devices. Flexible electronics provide a platform for device and sensor integration and packaging, which enables Internet-of-things (IoT) network applications.

**Keywords:** flexible; pH sensor; iridium oxide; roll-to-roll; sustainable



**Citation:** Chawang, K.; Bing, S.; Chiao, J.-C. Printable and Flexible Iridium Oxide-Based pH Sensor by a Roll-to-Roll Process. *Chemosensors* **2023**, *11*, 267. <https://doi.org/10.3390/chemosensors11050267>

Academic Editor: Pi-Guey Su

Received: 4 March 2023

Revised: 20 April 2023

Accepted: 27 April 2023

Published: 30 April 2023



**Copyright:** © 2023 by the authors. Licensee MDPI, Basel, Switzerland. This article is an open access article distributed under the terms and conditions of the Creative Commons Attribution (CC BY) license (<https://creativecommons.org/licenses/by/4.0/>).

## 1. Introduction

Rapid progress in thin film processing and flexible electronics has increased the demands and applications for a low cost, simple manufacturing, a high throughput, and integration techniques [1–4]. Conventional semiconductor fabrications rely on ultraviolet lithography processes, which are costly and only accessible by large organizations. Devices developed in research laboratories or by startup companies are typically only made in small quantities, especially during the prototyping stages. However, the fundamental challenges lie in transferring the lab-scale fabrication techniques to high-throughput industrial-scale manufacturing when the products go to mass production [4]. Roll-to-roll (R2R) fabrication processes were improvised for their simplicity with lower capital equipment expenses [5–8], higher throughputs [9], and a cost-effective alternative for printing lab-on-a-chip (LoC) devices [10–12].

The R2R process requires a substrate to roll and flex, making the paper- and polymer-material substrates desired choices. Notable electronics manufactured by R2R techniques are flexible solar cells, LEDs, and fuel cells [13–16]. The flexible substrates enable large-scale solar energy harvesters [17], radio frequency identification (RFID) antenna printing, and chip

bonding in commercial applications [18]. For example, Wang et al. developed a paper-based RFID antenna to enable Internet-of-things (IoT) applications [19]. Microchannels and arrays can also be patterned by R2R processes [20,21], and Liedert et al. demonstrated microfluidic devices that were developed on polymer films [22]. Electrochemical sensors developed by the R2R process were reported for glucose and carbofuran detection [23,24]. Martin et al. reported a wearable microfluidic device for sweat sampling from the epidermis layer [25], and similar applications were reported by other groups for skin applications [26,27].

With the growing demands for disposable electrochemical sensors, R2R techniques provide the advantages of lower manufacturing costs and a quick means to reconfigure fabrication materials and/or printing patterns and ensure uniform deposition. For disposable sensors, paper and polymer substrates are preferred for their cost-effectiveness, flexibility, and/or conformability on skin or in clothing and textiles [28,29]. Paper-based substrates require a low temperature budget. Selective laser sintering and photonic curing help to achieve higher conductivities at low temperatures but operate on a high amount of power [30–33]. New deposition methods with wet plating at room temperature overcome such limitations [34–36]. Iridium oxide ( $\text{IrO}_x$ ) was synthesized as an  $\text{H}^+$ -ion selective membrane for targeted applications [37]. The wide pH-sensing range and inert properties of  $\text{IrO}_x$  are advantageous for the bioelectrode for wearable, implantable [38–42], and harsh-environment sensing electrodes [43]. Experimental studies showed Nernstian to super-Nernstian responses of  $\text{IrO}_x$  fabricated by radio-frequency (RF) sputtering [44–46], electroplating [47–49], and sol-gel processes [50,51]. RF sputtering uses high-purity targets, and the sputtered material falling outside the substrate region is wasted. For electroplating and sol-gel, material waste is minimized as the deposition quantity is equal to consumption. Electroplating allows the conformal deposition of metal and oxide layers on fabric-like materials [52,53]. However, nanoparticle colloid suspensions used as coating solutions are operation-intensive. Sol-gel is an inexpensive coating process and allows for thin-film deposition on flexible substrates such as textiles [54–56] and polyimide [57,58]. Multiple coatings can be easily applied for thicker layers without adding additional facility costs. The economical coating process with sol-gel for flexible and large-area substrates provides fundamental compatibility for scaling. Oxidation after the coating is applied to convert the materials; thus, the thermal tolerance of the substrate should be taken into consideration.

Our group previously demonstrated flexible  $\text{IrO}_x$ -based pH sensors that were produced by a lab-scale sol-gel process on flexible polyimide films with a glass-transition temperature of 400 °C [57,58]. This manuscript reports the pH performance produced by a R2R process compatible with industry-scale manufacturing methods. Previously, dip coating in the sol-gel solution was used, which did not require vacuum or spinning apparatuses. The dipping tank can be scaled with the film substrate's size. Robotic arms to control the dipping speed and multiple repeated dip-and-dry processes were utilized to reach the desired thickness and uniformity [57,58].

The R2R process aims to produce a uniform  $\text{IrCl}_3$  layer to be converted to  $\text{IrO}_x$  by oxidation. The  $\text{IrO}_x$  film is used as a working electrode (named KWE) for pH sensing. This work presents the pH characterization of the planar electrodes that were mass-produced on flexible polyimide films by R2R against reference electrodes, named KREs. Prepared with the stencil printing technique, a layer of Ag/AgCl paste was applied on the same polyimide substrates. Ag/AgCl offers stable potentials and is a sustainable material, since it can be reused and recycled with negligible toxicity after treatment [59]. Such an automatic stencil technique is preferred for microelectronic packaging because of its use without waste and high throughputs [60].

The low-cost perspective of R2R-fabricated devices enables disposable sensors for point-of-care diagnostics [61–63]. The  $\text{IrO}_x$  and Ag/AgCl electrode pair on a flexible planar substrate can be used for non-invasive pH sensing on the skin or minimally invasive probing of a tissue's pH, besides their uses in portable point-of-care sensing devices or instruments as a replaceable element.  $\text{IrO}_x$  and Ag/AgCl are also versatile and stable as base electrodes for biomarker sensing, such as sodium chloride, lactic acid, L-glutamate,

and dopamine [64–68]. With the advances in R2R-fabricated electronics such as RFID, energy harvesters and storage, sensing electrodes made by R2R have great promise for integration into flexible systems that can address a variety of applications.

Potentiometry studies of the  $\text{IrO}_x$ -based KWE against a commercial glass-rod reference electrode (named CRE) were conducted in standard buffer solutions for confirmation. Commercial glass-rod-based reference electrodes are non-disposable, per a standard method, which was used to characterize the  $\text{IrO}_x$  KWE alone. Applications utilize the  $\text{IrO}_x$  KWE and Ag/AgCl KRE pairs. Initial cyclic voltammetry (CV) and potentiometry analysis were in the pH range of 5–8, targeting biological applications such as skin pH sensing [69–71], which validated their sensing performance. Sensitivity, hysteresis, stability, cationic interferences, and temperature dependence were investigated for the electrode pairs. Electrodes were then packaged in a flexible and bendable plastic material, so they can conform to the skin for pH sensing. The packaged electrodes were tested in artificial sweat to detect pH changes for sweat monitoring applications. Biofluids, especially from skin wounds, such as plasma, serum, and blood are viscous [72–74]. The devices were then tested in viscous solutions for a repeatability investigation. The performance results were illustrated in the Clarke error grids to show their reliability.

## 2. Materials and Methods

### 2.1. Roll-to-Roll Printing

Polyimide-based working electrodes were prepared by a roll-to-roll (R2R) process, which allows for high throughput and material-use efficiency. The precursor solution was prepared by mixing iridium (IV) chloride hydrate (Sigma Aldrich, St. Louis, MO, USA) with ethyl alcohol (Supelco, Bellefonte, PA, USA) and acetic acid (80%, LabChem, Zelienople, PA, USA), as illustrated in Figure 1a. The polymeric film was obtained from Sheldahl (Northfield, MN, USA). Base metal layers of gold (Au) and copper (Cu) with thicknesses of 90 nm and 18 nm, respectively, were deposited on flexible polyimide (125  $\mu\text{m}$  thick) that has a glass-transition temperature of 400  $^\circ\text{C}$ . Iridium oxide ( $\text{IrO}_x$ ) was used as the pH-sensitive film prepared by the sol-gel process.

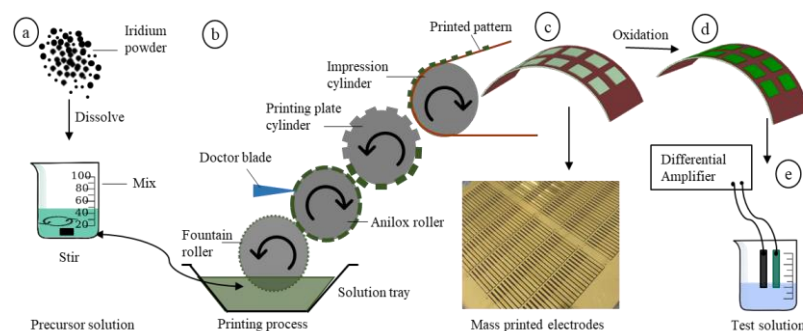


**Figure 1.** The manufacturing process of  $\text{IrO}_x$  pH sensors by roll-to-roll (R2R) process involves several steps: (a) precursor solution, (b) printing process on polyimide substrate with gold as a conductive layer, (c) picture of mass-printed electrodes, (d) oxide layer formation, and (e) tests in different solutions.

Figure 1b shows a type of R2R technique, known as the flexographic process, that was adopted for thin-film layer printing [75,76]. A 125  $\mu\text{m}$  thick carrier foil was used to enhance registration accuracy on the flexible polyimide. The anilox roller had a cell transfer volume of 5  $\text{mL}/\text{m}^2$  with a 5  $\text{m}/\text{min}$  printing speed for layer evenness. A plate size of 25  $\times$  240  $\text{mm}^2$  allowed for printing 480 electrodes per sheet with an electrode size of 2  $\times$  15  $\text{mm}^2$ . The printing processes were conducted in VTT Technical Research Centre of Finland Ltd., which was contracted with SensTek LLC in Oakland, CA, USA. The mass-printed samples shown in Figure 1c were oven-dried at 120  $^\circ\text{C}$  for 1 h. A programmable oven was used to ramp up the temperature to 325  $^\circ\text{C}$ , at a rate of 1  $^\circ\text{C}/\text{min}$  for oxide formation, as shown in Figure 1d.

Samples were heated at 325 °C for 4 h with an external meter to monitor temperature fluctuations. After the oxide formation, the sample was cooled to room temperature at the same cooling rate of  $-1$  °C/min. The IrO<sub>x</sub> layer thickness was estimated to be 800 nm, which was measured at multiple points using a surface profilometer (Veeco Dektak, Allentown, PA, USA). Material characterization by surface electron microscopy (SEM) of IrO<sub>x</sub> film developed at 325 °C was previously reported by our group [77].

The reference electrodes (KREs) were prepared by an automated stencil method on the same polyimide film with Au and Cu deposited. A stainless steel doctor blade with a moving speed adjusted to 1 inch/s at a 45° angle was used across the stencil. Commercial Ag/AgCl paste (ASLCo, Tokyo, Japan) was stencil-printed on a 6'' × 6'' flexible polyimide sheet. The samples were then heated to 120 °C for 10 min to dry. The measured thickness of the film was 13 μm. The KWE and KRE electrodes were individualized from the mass-printed batch by a singulation process. A laser-cutting machine protoLaser (LPKF R4, Naklo, Germany), adjusted to a speed of 500 mm/s and a channel width of 200 μm, produced electrode sizes of 2 mm × 15 mm. The stencil process was conducted at the NextFlex Technology Hub in San Jose, CA, USA, which was contracted by SensTek LLC (Oakland, CA, USA). Silver epoxy (MG Chemicals, Ottawa, ON, Canada) was used to attach copper wires on the gold surface of the electrodes for signal transduction. The electrodes were connected to analog input pins of a data acquisition device (National Instruments, Austin, TX, USA) for electrical measurements, as shown in Figure 1e.

## 2.2. Materials and Tools

Standard buffer solutions (Fisher Scientific, Waltham, MA, USA) of different pH levels were used during the electrochemical and pH characterization studies. Custom-made buffers were prepared by adding sodium chloride salt (NaCl) (Sigma, St. Louis, MO, USA) into standard buffers. Two types of custom-made buffers were prepared: pH solutions with the same salt concentration of 0.05 M NaCl salt and salt-added solutions with the same conductivity of 46 mS/cm. The purpose was to achieve a more stable output reading by increasing solution conductivity. A digital benchtop meter (Orion, Fisher Scientific, Waltham, MA, USA) was used for pH and conductivity measurements. Potassium chloride (KCl) (LabChem, Zelienople, PA, USA) and magnesium chloride (MgCl<sub>2</sub>) (Sigma, St. Louis, MO, USA) salts were used for cation interference in the selectivity study. A digital thermometer (Elitech, San Jose, CA, USA) was used to track temperature change from 3.8 °C to 50 °C. Cyclic voltammetry analysis (CV) was performed in a three-electrode cell system using an electrochemical analyzer (CH Instruments, Bee Cave, TX, USA). A commercial glass-rod Ag/AgCl reference electrode (Basi, West Lafayette, IN, USA) filled with 3 M NaCl solution was utilized for CV experiments and working electrode investigation.

A thermal laminator (Amazon, Seattle, WA, USA) was used to package the electrodes and create insulation wells around the sensing area. Electroanalytical tests were performed on laminated sensors using artificial sweat (Reagents, Belmont, NC, USA) with an original pH value of 4.7. The artificial sweat was made of sodium bicarbonate (NaHCO<sub>3</sub>), NaCl, potassium carbonate (K<sub>2</sub>CO<sub>3</sub>), and traces of lactic acid (C<sub>3</sub>H<sub>6</sub>O<sub>3</sub>), urea (CH<sub>4</sub>N<sub>2</sub>O), and acetic acid (CH<sub>3</sub>COOH). The abundance of ionic concentration was, therefore, expected to produce a discrepancy in output potentials compared to buffer solutions that are mostly made from phosphate groups. Hydrochloric acid (HCl) (LabChem, Zelienople, PA, USA) and sodium hydroxide (NaOH) (Sigma-Aldrich, St. Louis, MO, USA) were used to change pH values. Starch powder (Carolina, Burlington, NC, USA) was used to create viscous fluids, and a viscometer tube of size 200 (CANNON, State College, PA, USA) was used for viscosity measurements.

## 3. Results and Discussion

### 3.1. Performance of the Polyimide-Based Working Electrode

Figure 2a shows the potential responses of the R2R IrO<sub>x</sub> KWE tested against a commercial reference electrode (CRE). Each test lasted for 1 min in standard buffer solutions from

pH 2 to 13. Electrodes were cleaned in deionized (DI) water before every pH test, which was intended to remove residues that may change the electrochemical equilibrium. To investigate fabrication uniformity, three KWE electrodes (S1, S2, and S3) were continuously tested for two cycles. One cycle means tested in a sequence from acid to alkaline and back to acid in the order of pH 2-4-7-10-13-10-7-4-2. In Figure 2a, all three electrodes demonstrated similar output potentials in different pH solutions against the CRE. It should be noted that the CRE is assumed to produce identical reference potentials in all buffer solutions and with repeatability, when moved from one solution to another. However, in reality, the glass-rod membrane in the CRE may be affected by ionic residues when it was switched between different solutions. The potential variations were observed when two identical CREs were switched between buffer solutions. The ideal outputs should have been zero in all conditions, but the observed non-zero variations seemed to be random. Thus, it was concluded that the CRE may also contribute to some output variations, when used with the KWE. The KWE surfaces may also be affected by such ionic residues. These effects contributed to hysteresis, as defined in [77], and were observed in Figure 2a.

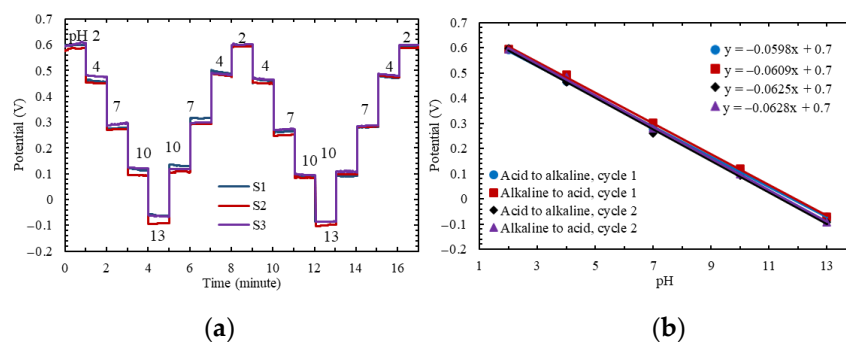


**Figure 2.** (a) Potential response of the R2R IrO<sub>x</sub>-based working electrode (KWE) vs. a commercial reference electrode (CRE). (b) Nernstian responses obtained from averaged potentials of 3 sensors tested in acid-to-alkaline and alkaline-to-acid sequences for two test cycles. One cycle here means tested in the sequence pH 2-4-7-10-13-10-7-4-2.

Overall, the temporal potential responses to pH were consistent for the three different IrO<sub>x</sub> electrodes. The sensitivities, tested in acid-to-alkaline or alkaline-to-acid sequences, for the two cycles are shown in Figure 2b. The output potentials from Figure 2a for S1, S2, and S3 were averaged in two individual cycles and used to obtain the sensitivities for different test sequences. A linear slope for the responses was assumed to be in the pH range of 2–13 and defined as the sensitivity. The electrode produced similar Nernstian responses regardless of the test sequence. The Nernstian behavior of IrO<sub>x</sub> films fabricated by dipping and oxidized at 325 °C was previously reported in detail by our group [68,77]. R2R printing produced similar results as dip coating. Due to better film uniformity, we observed better repeatability of the measurement results. For cycle 1, the sensitivities were  $-59.8$  and  $-60.9$  mV/pH, for the acid-to-alkaline and alkaline-to-acid tests, respectively, while, for cycle 2, they were  $-62.5$  and  $-62.8$  mV/pH, respectively. The slightly higher sensitivities for cycle 2 may be due to surface hydration, as the devices stayed in the solution longer. Madeira et al. demonstrated that hydrated films produced higher Nernstian responses compared to dehydrated films [78]. The pH-sensing mechanism for an amorphous IrO<sub>x</sub> film was reported to exhibit Nernstian responses depending on the degree of hydration [79,80].

Hysteresis (dV), as previously defined in [77], is the standard error of the settled potentials measured at the same pH level in one cycle, as illustrated in Figure 3a. Since the responses might have drifts in potential from the moment the electrodes were immersed in a solution, the outputs were compared with fixed time points after the electrodes were switched. The recording was at seven samples per second and continued for one minute in each solution. With the data obtained from Figure 2a, at the 6th s after the electrodes were moved from the previous solution to a new one, Figure 3b shows a higher level of

hysteresis in the alkaline range. The “ $\pm$ ” ranges were calculated with respect to the average of three output potentials at a specific pH level for the individual sensor. This can be explained by the slower diffusion of the larger  $\text{OH}^-$  ions at the buried sites compared to that of the  $\text{H}^+$  ions [81]. Hysteresis has been reported in other metal oxides [82–86]. For example, a higher  $dV$  in the alkaline region was also observed using  $\text{Al}_2\text{O}_3$  metal oxide as a sensing film [87]. The highest  $dV$  at pH 7, particularly for S1, can be explained by the equal numbers of  $\text{OH}^-$  and  $\text{H}^+$  groups in the solution counteracting on the electrode surface, which was also previously observed for porous polypropylene membranes [88]. If any residue of the  $\text{OH}^-$  and  $\text{H}^+$  groups was left on the surface from the previous solution before the electrodes entered pH 7, the additional residues produced a more obvious effect of hysteresis. The output potential at a specific pH level was used with the sensitivity curve to find the  $d\text{pH}$  from the  $dV$ . Among the three electrodes, the highest pH change ( $d\text{pH}$ ) produced by hysteresis ( $dV$ ) at pH 2, 4, 7, 10, and 13 were 0.1, 0.2, 0.3, 0.32, and 0.25, respectively. In a wide pH range of 2–13, hysteresis ( $dV$ ) did not create a drastic pH change and showed good repeatability. The electrode after continuous tests at pH 2 and 13 showed good repeatability of the Nernstian response.

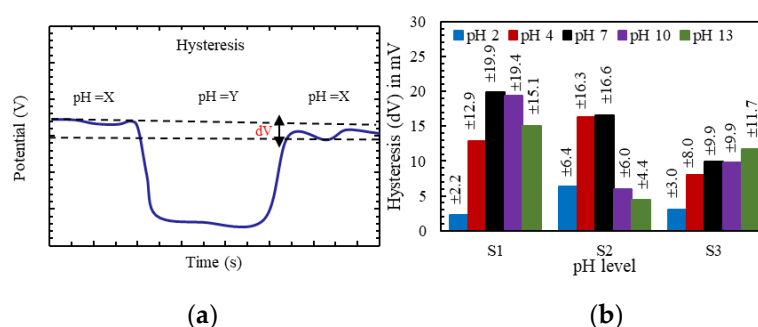


**Figure 3.** (a) Definition of hysteresis ( $dV$ ). (b) The highest hysteresis potentials of individual electrodes between cycle 1 and cycle 2.

### 3.2. Cyclic Voltammetry Analysis

Cyclic voltammetry (CV) analysis was performed in a commercial phosphate buffer solution (PBS) with a pH value of 7.4 and salt ( $\text{NaCl}$ ) concentrations of 0.137 M  $\text{NaCl}$ . The reason to use PBS that contained  $\text{NaCl}$  was to validate the electrode voltammetry performance in a solution related to biological environments. KWE was used as the working electrode (WE), and a platinum foil with a diameter of 1.3 cm was used as the counter electrode (CE). The potential sweeps were between  $-0.8$  V to  $+1$  V at a scan rate of 30 mV/s. Figure 4a,b show the CV curves of KWE against the rigid commercial reference electrode (CRE) and the flexible  $\text{Ag}/\text{AgCl}$  KRE electrode.

Figure 4a shows the results of the case when the KWE was tested from its dry state before it was submerged into the PBS solution. Figure 4b shows the results of the case when the KWE was placed in the buffer pH 2 solution for 30 min before it was switched to PBS. The pH 2 solution served as a precondition to mimic a hydrated and used electrode. The similar voltammograms of KWE vs. KRE compared to KWE vs. CRE in Figure 4 show that the flexible polyimide KRE electrodes paired with  $\text{IrO}_x$  KWE can generate sufficient electrical currents, similar to the glass-rod CRE. Similar curve shapes during the anodic and cathodic scans suggest reversible electrochemical mechanisms. A comparison of Figure 4a,b shows preconditioning at the strong pH 2 level does not change the electrochemical equilibrium.

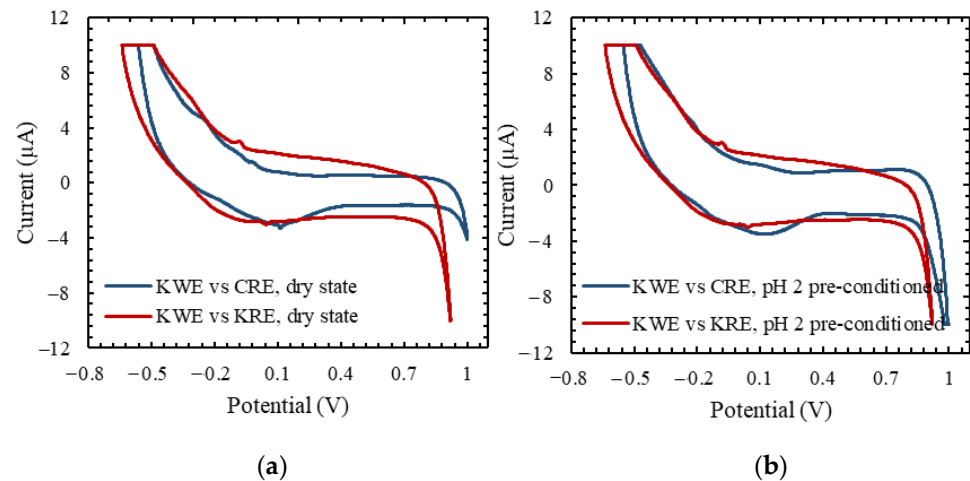


**Figure 4.** KWE vs. CRE and KWE vs. Ag/AgCl KRE in phosphate buffer solution (PBS) tested from (a) dry state and (b) preconditioned at pH 2.

3.3. Analytical Characterization of KWE vs. KRE

The KWE vs. KRE pairs were tested for two cycles in custom-made buffer solutions from pH 5 to pH 8. Electrodes were first tested in these buffers with the same salt concentration of 0.05 M added to prevent unstable potential readings due to low solution conductivity in the commercial buffer solutions. Each cycle was tested in the sequence of 5-6-7-8-7-6-5. The pH range was limited because of targeted applications in biologically relevant solutions, particularly for sensing on the skin. The distance between electrodes was fixed at 2 mm. Electrodes were again tested for one minute and were cleaned in deionized (DI) water before every test intending to remove residues. The blue curve in Figure 5a indicates that the electrode pair was first preconditioned in a strong acid of pH 2, whereas the red curve indicates when the electrodes were tested from their dry state directly in a pH 5 solution. Both types of tests showed distinct potentials in every pH test with good consistency. It was noted that pH 5 and 6 potentials became the same as their respective values after the first half cycle, as the electrodes experienced hydration in the first two tests, although the outputs at pH 5 and 6 for the first two tests showed larger differences. The inset shows a Nernstian response of  $-60.6 \text{ mV/pH}$  in the pH range from pH 5 to 8 for both the dry and preconditioned electrodes.

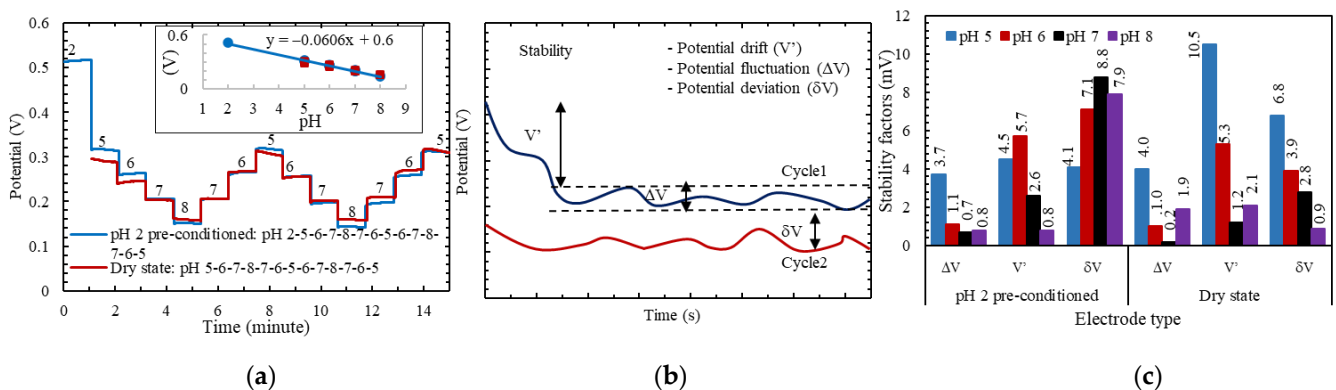


**Figure 5.** (a) Potential response of KWE vs. KRE in pH 5 to 8 custom-made buffers after the electrode was preconditioned at pH 2 (blue) and from a dry state (red). The inset shows a Nernstian response with good linearity. (b) The definition of stability is categorized by  $V'$ ,  $\Delta V$ , and  $\delta V$ . (c) The highest  $V'$ ,  $\Delta V$ , and  $\delta V$  for pH 2 preconditioned and dry-state cases.

Stability is a practical issue caused by inherent factors such as fabrication processes and random factors such as vibrations in the micro-environment. Poor stability produces

measurement errors and compromises pH accuracy. Huang et al. previously categorized potential stability into the parameters of potential fluctuation ( $\Delta V$ ), potential drift ( $V'$ ), and potential deviation ( $\delta V$ ), as illustrated in Figure 5b [77].  $\Delta V$  is defined as the maximum potential fluctuations within a measurement period. It is typically in a small range, which may be caused by vibrations and fluidic disturbance after the electrodes are switched in solutions.

Drift ( $V'$ ) is defined as the time-dependent change between the initial and stabilized potential values. It was reported that it was caused by oxidation states on the metal oxide electrode surface and the interactions of electrochemically active species such as oxygen in solution [89,90]. Deviation ( $\delta V$ ) is defined as the potential difference between two cycles tested at the same pH levels. It is different from hysteresis ( $dV$ ), which is defined as the potential difference at the same pH levels for the same test cycle.

Figure 5c shows the stability, as defined by  $\Delta V$ ,  $V'$ , and  $\delta V$  in Figure 5b. The KWE–KRE electrode pairs produced the highest  $\Delta V$ ,  $V'$ , and  $\delta V$  of 3.7 mV, 4.5 mV, and 8.8 mV, respectively, for the preconditioned (at pH 2) electrodes, and of 4 mV, 10.5 mV, and 6.8 mV, respectively, for the electrodes initially at the dry state. The measured values were comparable with the previously reported values of 1 mV, 10 mV, and 5 mV for IrO<sub>x</sub>-Ag/AgCl by the sol-gel dipping method [77]. With an averaged sensitivity of  $-60.6$  mV/pH,  $\Delta V$ ,  $V'$ , and  $\delta V$  correspond to pH variations of 0.06, 0.07, and 0.15, respectively, for the precondition state, and of 0.07, 0.2, and 0.13, respectively, for the dry state. Initial tests in different pH solutions may cause output changes, even in equilibrium, possibly due to charge variations on the electrode surface [91]. The low pH variations from  $\Delta V$  and  $V'$  mean our planar IrO<sub>x</sub>-Ag/AgCl electrodes can distinguish small changes. Similarly, the low pH variation for  $\delta V$  shows good repeatability between different test cycles for the roll-to-roll fabrication processes.

Two new pairs of electrodes were separately tested in pH from 2 to 7 and pH from 13 to 7, with salt added to adjust the solution conductivities to be the same at 46 mS/cm. In the commercial pH buffer solutions, due to different compositions, their conductivities are widely different. The value of 46 mS/cm was chosen because the highest conductivity of all the buffer solutions we used in the tests was 46 mS/cm. The electrodes were tested for two cycles. The purpose was to investigate linearity in a wider pH range of pH 2–13. Solutions with low conductivity specifically affected linearity in a wide pH range because individual output potential in a certain solution depended on its conductivity. For the comparisons to be fair, the conductivities were equalized. The arrows in Figure 6 indicate the different test sequences. The blue arrow indicates the test starts at pH 2, and the purple arrow indicates the test starts at pH 13.

The sequences were 2-4-5-6-7-6-5-4-2 and 13-11-10-8-7-8-10-11-13. Then, each sequence was repeated for a second cycle. The result from Figure 5a was also included, which had two-cycle sequences of 5-6-7-8-7-6-5. The experiments were also to examine the inferences of OH<sup>-</sup> and H<sup>+</sup> on the surface as residues in acidic and alkaline environments, respectively. Figure 6 shows a good linear fit in the pH range of 5–8 (blue), pH range of 2–7 (green), and pH range of 13–7 (purple). The data labels overlapped with each other at the same pH because of high repeatability. The differences in these groups are more at pH 7 and 8. This phenomenon might be due to the ionic interference on the surface, as it went through OH<sup>-</sup>- or H<sup>+</sup>-dominating solutions before pH 7 or 8. The measured hysteresis ( $dV$ ) for the individual electrode pairs tested at pH 2, 4, 5, 6, and 7 was  $\pm 7$  mV,  $\pm 7.2$  mV,  $\pm 3.2$  mV,  $\pm 2.4$  mV, and  $\pm 0.1$  mV, respectively. In the alkaline range, at pH 13, 11, 10, 8, and 7, the  $dV$  was  $\pm 6.8$  mV,  $\pm 9.5$  mV,  $\pm 8.8$  mV,  $\pm 7.3$  mV, and  $\pm 5.2$  mV, respectively. The measured  $dV$  for the skin pH range of pH 5, 6, 7, and 8 was  $\pm 2.1$ ,  $\pm 1.1$ ,  $\pm 0.1$ , and  $\pm 3.9$  mV, respectively, for the pH 2 preconditioned cases, and  $\pm 3.4$ ,  $\pm 7.7$ ,  $\pm 4.1$ , and  $\pm 0.4$  mV, respectively, when tested from the dry state. The hysteresis was evaluated within the same cycle. However, two hysteresis values were obtained for two cycles, and the values presented above were the larger ones. Again, the “ $\pm$ ” range of the hysteresis was obtained from the maximum and minimum values with respect to the average value of the output potential for a specific pH.

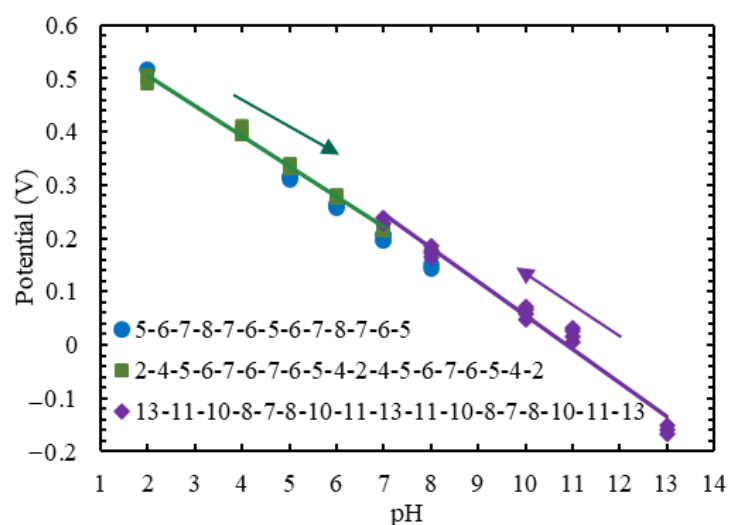


**Figure 6.** Linear fits for tests at skin pH range of 5–8 (blue), in acid pH range of 2–7 (green), and alkaline pH range of 13–7 (purple), tested for two cycles in custom-made buffers.

### 3.4. Selectivity to Cationic Interference

To study the selectivity of our electrode, three types of interference cations were added to the 50 mL custom-made buffer solutions prepared with the same salt concentration. Figure 7 shows the potential responses without additional cationic interference and with 0.1 M additions of NaCl, KCl, and MgCl<sub>2</sub>.

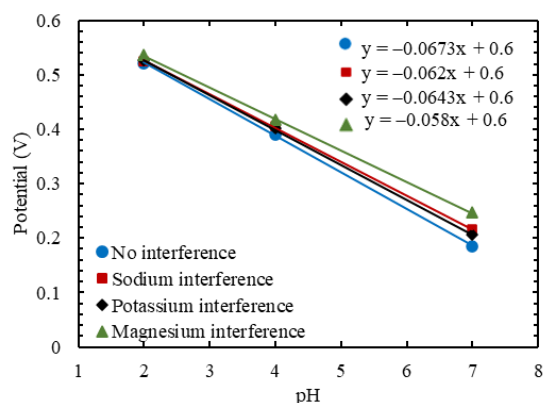


**Figure 7.** Measured sensitivities without cationic interference and with additional 0.1 M sodium, potassium, and magnesium cations.

The electrode pairs of KWE–KRE were tested at pH 2, 4, and 7 for one minute and cleaned in DI water before the next test. Additional ions created potential shifts, specifically at pH 7, but the Nernstian responses were maintained. The increases in output potentials can be explained by the solution pH changes. At pH 2, the abundant H<sup>+</sup> ions made the presence of additional Na<sup>+</sup>, K<sup>+</sup>, and Mg<sup>2+</sup> insignificant. However, at pH 7, the additional positive-charged ions made the solution seem more acidic and shifted the output potential, specifically for the MgCl<sub>2</sub> case. The measured pHs by the commercial pH meter with 0.1 M NaCl, KCl, and MgCl<sub>2</sub> added in the pH solution became 6.8, 6.79, and 6.24.

### 3.5. Effect of Temperature

The IrO<sub>x</sub>-Ag/AgCl electrode pairs were tested at four temperatures, 3.8 °C, 22 °C, 37 °C, and 51 °C, and at three pH levels, 2, 4, and 7. The solution temperatures were monitored by immersing a probe connected to a temperature data logger (Elitech, San Jose, CA, USA) in solutions that were heated or cooled in a water bath. The electrodes were

tested for one minute and cleaned in DI water. Figure 8a shows that the output potential monotonically decreases as the temperature increases, as indicated by the arrows at three pH levels. The temperature dependency matches the redox mechanism in [77]. Figure 8b shows temperature coefficients of  $-2.1$ ,  $-2.9$ , and  $-3.1$  mV/°C measured at pH 2, 4, and 7, respectively, compared to the previously reported theoretical values of  $-0.3$ ,  $-0.8$ , and  $-1.3$  mV/°C, respectively, and the measured values of  $-2$ ,  $-0.3$ , and  $-0.7$  mV/°C, respectively, for the IrO<sub>x</sub> electrodes made by sol-gel dipping in our group [77]. The difference may be due to the different oxide states and the linear fitting of limited data in [72]. The sol-gel dipping method created random nanoscale and microscale pores that may affect heat dissipation on the film surface, producing different oxide states. Different groups also reported similar values:  $-1.27$  and  $-2$  mV/°C for IrO<sub>x</sub>- and palladium oxide (PdO)-sensing films, respectively [92,93].

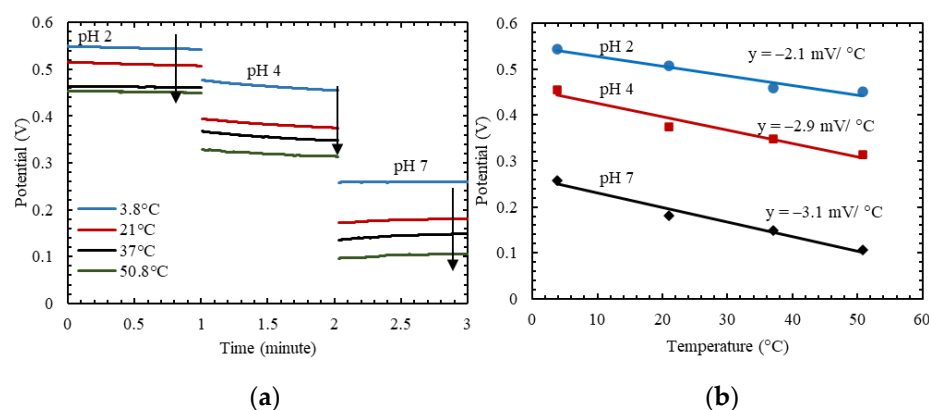


**Figure 8.** (a) Potential responses at three pH and four temperature levels. Arrows indicate potential monotonically decreases as temperature increases. (b) The inset shows temperature coefficients at pH 2, 4, and 7.

### 3.6. Laminated Electrodes

Packaging R2R-made electrodes can utilize the advantage of the same R2R processes such as lamination that can be integrated into the manufacturing flow. Laminating sheets and double-sided sticky tape of thicknesses 76  $\mu\text{m}$  and 114  $\mu\text{m}$  were stacked as the packaging and insulation layers. A packaged device within these layers is shown in Figure 9a. A mechanical punch with a diameter of 2 mm was used to puncture holes and open the sensing areas. The microwell depth was 114  $\mu\text{m}$ . The KWE and KRE electrodes were on the same substrate, with a spacing of 2 mm. The assembly films were passed through a thermal laminator, as shown in Figure 9b. The process is suitable for large-scale films and can be integrated into electrode-manufacturing processes. After batch processes, each packaged device can be individualized by cutting with a sharp blade. The overall manufacturing method is cost-effective, without the requirements of a vacuum environment or wafer transfer. The use is illustrated in the cross-sectional views in Figure 9c,d, which show how pH sensing is performed. Due to the flexibility of the substrate and packaging films, the sensor can conform to a curved surface such as human skin. We estimated that a volume of 300  $\mu\text{L}$  sample solution dripped from a pipette on the microwells is needed to cross over the wells for performance evaluation. A leak test was conducted to ensure that the insulating tape can prevent the liquid from shorting the connection lines to the IrO<sub>x</sub> and Ag/AgCl electrodes.

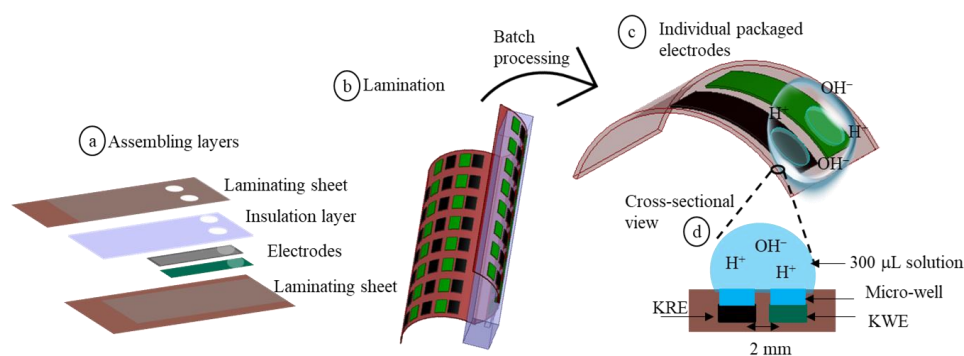


**Figure 9.** (a) Electrode assembling process with open sensing areas, (b) lamination of electrode assembly, (c) individual packaged electrodes after batch processing, and (d) cross-sectional view of the pH-sensing protocol.

The laminated electrodes were tested under their flat and curved conditions. The device in the curved condition was conformed on a plastic arc that had a curvature radius of 8.5 mm. The sample liquid was dripped onto the overall sensing area, and the output potentials were recorded for one minute in both conditions. DI water and medical cotton wipes were used to clean and dry the device between the two solutions. A drop of liquid stayed at the top of the arc to prevent it from sliding down. Figure 10a shows similar potential responses at pH 2–7 for two cycles. One cycle here means a sequence of pH 2-4-5-6-7-6-5-4-2. The Nernstian responses were  $-63.2$  and  $-63.6$  mV/pH for the flat and curved conditions, respectively, as shown in Figure 10b. The device performed similarly when it was bent. The plot in Figure 10b contains all the individual data points for two cycles, with them overlapped at the same values. The hysteresis (dV) values were obtained from the same pH in the first or second cycles. The hysteresis potentials and their corresponding pH variations (dpH) were calculated for two cycles, as shown in Table 1. The calibration curve obtained from the output potentials and solution pHs was used to calculate the dpH. The dpH was in the range of 0.08–0.1, which was caused by dV for the pH range of 2–7. The stability values categorized by  $\Delta V$ ,  $V'$ , and  $\delta V$  were calculated for the worst cases, meaning the largest values among all conditions, as shown in Table 1. The highest pH variations from pH 2 to 7 caused by potential fluctuation ( $\Delta V$ ), potential drift ( $V'$ ), and potential deviation ( $\delta V$ ) were 0.009, 0.09, and 0.1 mV, respectively, and in the worst cases were 0.6, 6.3, and 6.9 mV, respectively. The worst pH variation among all cases of dV,  $\Delta V$ ,  $V'$ , and  $\delta V$  in Table 1 is pH 0.1, which means that packaged electrodes can accurately detect changes as small as pH 0.1 in aqueous solutions. The similar sensitivities, low hysteresis, and good stability indicated by the values validate this reliable fabrication process.

To further investigate the performance of the packaged sensors in practical scenarios, the electrodes were tested in artificial sweat (Reagents, Charlotte, NC, USA) with the pH levels adjusted from pH 4 to 9 by adding HCl or NaOH. The original pH value of the artificial sweat was 4.7 and contained 185 mM of NaCl. To compare, the average NaCl concentration in sweat is 40–60 mM [94]. The pH values of the adjusted artificial sweat were measured by a commercial pH meter (Orion, USA). The artificial sweat was used as a control material because it was not possible to ensure the uniformity of human sweat from different persons or at different times. The tests were repeated five times at each pH to gather statistically meaningful data. The Test1 data were used to establish a linear calibration curve to find pH values for the measured potentials for Test2–Test5. The data were analyzed in the Clarke error grid shown in Figure 11. All the pH values fall in region A, showing an acceptable accuracy of the laminated R2R electrodes. The inset shows distinct responses at pH 4, 4.5, 5, 5.5, 6, 6.5, 7, 8.2, and 9. Each test lasted for 30 s after the respective solution was dripped on the sensing site. The potential responses for artificial sweat were higher than the values in the buffer solutions due to the higher ionic concentrations with added salt. For example, at pH 4, the output potential in artificial sweat

was 0.48 V, compared to 0.37 V in buffer pH 4. The inorganic elements in artificial sweat, NaHCO<sub>3</sub> and K<sub>2</sub>CO<sub>3</sub>, had concentrations of 0.11 M and 3.473 mM, respectively. They also increased the conductivities of the solutions and induced higher output potentials. In practical applications, the shifted output potentials caused by salts at known concentrations can be calibrated to achieve better accuracy, as previously demonstrated in aqueous and viscous solutions [95].

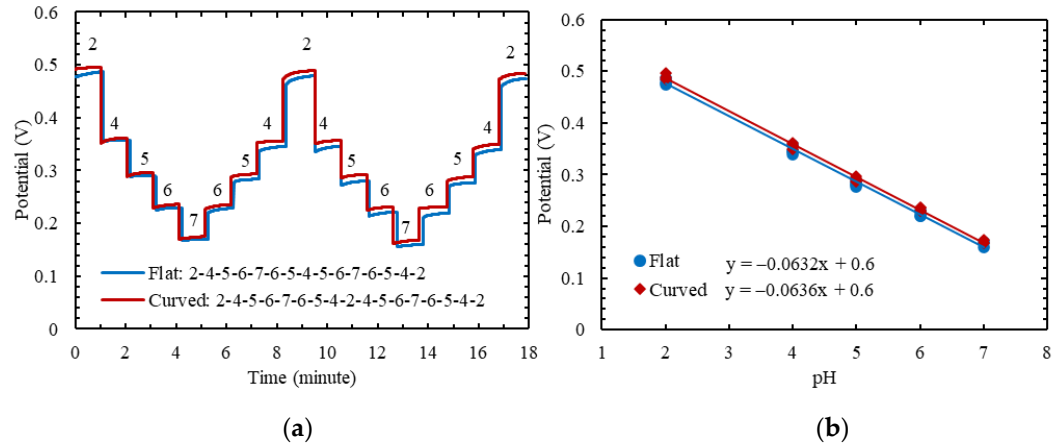


**Figure 10.** (a) Potential responses for flat and curved conditions from pH 2 to 7, and (b) corresponding sensitivities.

**Table 1.** Hysteresis (dV), pH variation (dpH), and stability.

pH	Cycle 1		Cycle 2		ΔV	Stability in mV	
	dV (mV)	dpH	dV (mV)	dpH		V'	δV
2	±5.7	0.09	±5.5	0.09	0.3	6.3	4.3
4	±6.0	0.09	±6.5	0.1	0.2	3.1	6.9
5	±4.9	0.08	±6.0	0.1	0.3	2.3	4.0
6	±3.4	0.05	±5.5	0.09	2.0	2.8	0.3
7	±5.3	0.08	±5.3	0.08	0.6	2.6	6.0

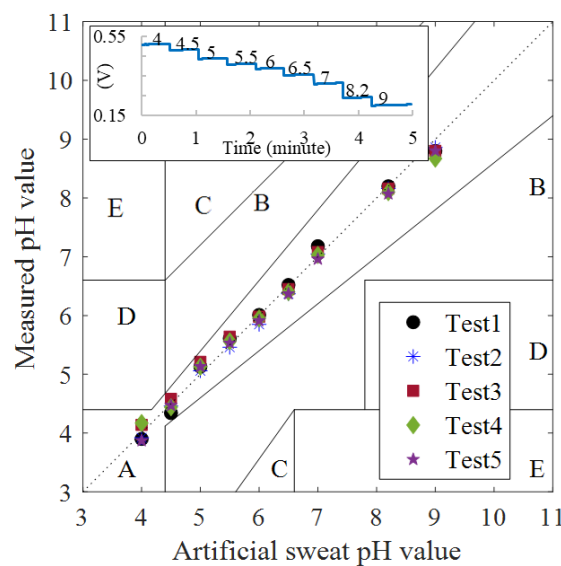


**Figure 11.** Clarke error grid assessment for packaged electrodes in artificial sweat pH measurement, where Test1 is the calibration standard. Inset shows the distinct potential response for artificial sweat at pH 4, 4.5, 5, 5.5, 6, 6.5, 7, 8.2, and 9.

Previous studies showed liquid viscosity plays a role in pH sensing [96]. In addition to being bulky and unsuitable for wearables, conventional glass-rod pH meters face challenges with membrane clogging [97]. The planar electrode faces fewer issues, but viscosity-dependent solution conductivity inevitably changes the output potentials. The devices were tested in viscous solutions from pH 4 to 10 to investigate the responses of laminated R2R sensors. The buffer solutions were first heated to 90 °C, and starch powder was added to create a viscosity of 1.17 cP, which was close to the viscosity of human blood [98], as measured by a viscometer (CANNON, State College, PA, USA). Next, NaCl salt was added to the heated solution and mixed thoroughly to mimic the salt concentration of 154 mM (0.9%) in human blood [99]. The output potentials were converted to pH, and the results are shown in the Clarke error grid of Figure 12, with the inset showing distinct outputs at different pH values. It was expected that the viscous solution containing ions from the starch molecules changed the solution conductivities and affected the output potentials [100]. The spreads of the outputs were larger than those in aqueous solutions. The microwells in the laminated devices were also expected to conceal more residues, resulting in higher hysteresis. It was observed that the converted pH values of the last experiment data of Test3 became higher than those of Test2 and Test1. The highest pH error observed was about 0.5. This was likely due to the ionic viscous deposits trapped in the microwells. For application cases that monitor skin conditions, sudden changes in pH across a wide range may not occur, so the effects from previous pH-level residues are unlikely to create errors. However, the viscosity-added accumulation of salt in the packaged sensor may have a pH-drifting issue.

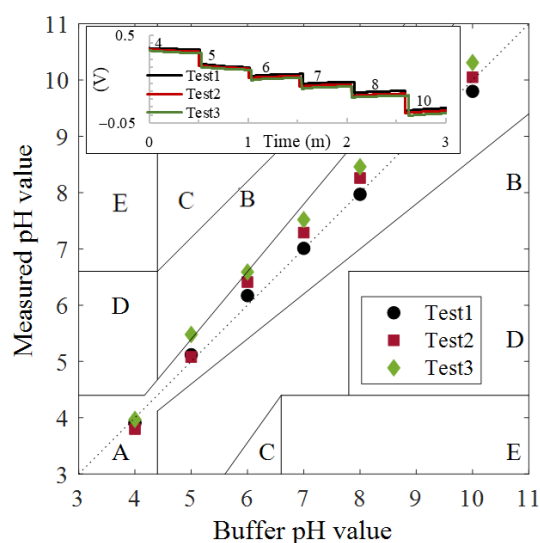


**Figure 12.** Clarke error grid assessment for packaged electrodes in viscous solution, where Test1 is the calibration standard. Inset shows the same potential response of the same electrode tested three times. All electrodes showed a distinct response at pH 4, 5, 6, 7, 8, and 10.

The pH-sensing performance of printing IrO<sub>x</sub> film by the R2R process is comparable with our previously reported values from the sol-gel dipping processes [77]. For the purpose of illustration, other exemplary pH sensors developed on conductive polymer materials [101–104] and metal oxides [105,106] from the literature show comparable sensitivities and linear ranges, as shown in Table 2. The sensitivity and linear range were defined by the respective authors. In addition to buffer solutions, some compared results with real-life samples. It should be noted that these reports were based on different testing conditions, protocols, and solutions, so the results shown are for reference only.

**Table 2.** pH-sensing performance reported in the literature.

Material	Sensitivity (mV/pH)	Linear pH Range	Sample *	Reference
IrO <sub>x</sub> <sup>1</sup>	−60.6	2–7 and 13–7	A.S. <sup>6</sup> V.S. <sup>7</sup>	This work
IrO <sub>x</sub> <sup>1</sup>	−(51.1–51.7)	1.5–12.1		[77]
PANI <sup>2</sup>	−58.7	5.45–8.62		[101]
PANI <sup>2</sup>	−60.3	2.1–12	Orange	[102]
PEDOT:BTB <sup>3</sup>	−(62–67)	4–7	A.S. <sup>6</sup>	[103]
PANI <sup>2</sup>	−50	4–10	Keratinocyte cells	[104]
WO <sub>3</sub> <sup>4</sup>	−377.5	6.9–8.94	A.S.W. <sup>8</sup>	[105]
RuO <sub>2</sub> /Al <sub>2</sub> O <sub>3</sub> <sup>5</sup>	−55.3	2–6	Beverages <sup>9</sup>	[106]

\* Samples used besides buffer solution. <sup>1</sup> Iridium oxide (IrO<sub>x</sub>) film developed on polyimide by thermal oxidation. <sup>2</sup> Polyaniline (PANI) on polymer substrates by wet chemical process. <sup>3</sup> pH-sensitive dye bromothymol electroplated on conductive poly(3,4-ethylenedioxythiophene):poly(styrene-sulfonate) (PEDOT:BTB) synthetic cotton and silk fibers. <sup>4</sup> Tungsten oxide (WO<sub>3</sub>) nanofiber with a differential amplifier. <sup>5</sup> Ruthenium oxide (RuO<sub>2</sub>) sputter-deposited on aluminum oxide substrate (Al<sub>2</sub>O<sub>3</sub>). <sup>6</sup> Artificial sweat (A.S.). <sup>7</sup> Viscous solution (V.S.). <sup>8</sup> Artificial seawater (A.S.W.). <sup>9</sup> Beverages include wine, juice, milk, tea, and others.

#### 4. Conclusions

This paper demonstrates a novel iridium oxide-based (IrO<sub>x</sub>) pH sensor manufactured by roll-to-roll (R2R) processes, compatible with the currently available high-throughput mass production equipment. The continuous printing process of R2R provides flexibility in scaling between lab-scale and industrial-scale production.

The fabrication and characterization of the IrO<sub>x</sub>-Ag/AgCl electrodes prepared by the R2R and stencil techniques showed good consistency among the different sensors. A linear sensitivity of −60.6 mV/pH was achieved with different ranges of pH and different testing sequences. Hysteresis (dV) investigated was ±7, ±7.2, ±3.2, ±3.5, ±5.2, ±7.3, ±8.8, ±9.5, and ±6.8 mV at pH 2, 4, 5, 6, 7, 8, 10, 11, and 13, respectively, corresponding to pH variations (dpH) of 0.1, 0.12, 0.05, 0.06, 0.08, 0.12, 0.14, 0.15, and 0.1. The stability issues were categorized by potential fluctuation (ΔV), potential drift (V'), and potential deviation (δV), and the worst pH variations of 0.07, 0.2, and 0.15, respectively, were found in the pH range of 5–8. The measured hysteresis and stability demonstrate the fabrication uniformity, reliability, and repeatability. The interference studies and temperature dependence are comparable with the previously reported values. The laminated electrodes were made with the same R2R procedures and tested in aqueous artificial sweat and viscous solutions. Analytical studies of the laminated electrodes under flat and curved conditions showed that the electrodes can be reliably used for skin pH sensing through further assessments in the Clarke error grids.

The fabrication process and materials are sustainable, as the sensing materials consumed are equal to those produced, so the waste is minimal. The reconfigurable, cost-effective, and scalable manufacturing method features advantages for disposable and integrated sensors, in which radio frequency integrated circuit (RFID) devices can be easily packaged with the electrodes to provide interfacing and communication functions. The sensing communication possibility opens new pathways for large-quantity deployment of Internet-of-things (IoT) systems.

**Author Contributions:** Conceptualization, J.-C.C.; methodology, J.-C.C. and K.C.; software, K.C.; validation, K.C. and S.B.; formal analysis, K.C.; investigation, K.C.; resources, J.-C.C.; data curation, K.C.; writing—original draft preparation, K.C.; writing—review and editing, K.C., S.B., and J.-C.C.; visualization, K.C.; supervision, J.-C.C.; project administration, J.-C.C.; funding acquisition, J.-C.C. All authors have read and agreed to the published version of the manuscript.

**Funding:** This research received no external funding.

**Institutional Review Board Statement:** Not applicable.

**Informed Consent Statement:** Not applicable.

**Data Availability Statement:** No public data disclosure.

**Acknowledgments:** The authors sincerely appreciate the facility and financial support from the Lyle School of Engineering and the generosity of Mary and Richard Templeton.

**Conflicts of Interest:** The authors declare no conflict of interest.

## References

1. Palavesam, N.; Marin, S.; Hemmetzberger, D.; Landesberger, C.; Bock, K.; Kutter, C. Roll-to-roll processing of film substrates for hybrid integrated flexible electronics. *Flex. Print. Electron.* **2018**, *3*, 014002. [CrossRef]
2. Machui, F.; Hösel, M.; Li, N.; Spyropoulos, G.D.; Ameri, T.; Søndergaard, R.R.; Jørgensen, M.; Scheel, A.; Gaiser, D.; Kreul, K. Cost analysis of roll-to-roll fabricated ITO free single and tandem organic solar modules based on data from manufacture. *Energy Environ. Sci.* **2014**, *7*, 2792–2802. [CrossRef]
3. Smolka, M.; Ruttloff, S.; Nees, D.; Prietl, C.; Satzinger, V.; Lamprecht, B.; Hütter, P.; Hesse, J.; Kokkinis, G.; Kriechhammer, G. High throughput roll-to-roll production of microfluidic chips. *Proceedings* **2018**, *2*, 1054.
4. Søndergaard, R.R.; Hösel, M.; Krebs, F.C. Roll-to-Roll Fabrication of Large Area Functional Organic Materials. *J. Polym. Sci. Part B Polym. Phys.* **2013**, *51*, 16–34. [CrossRef]
5. Cagnani, G.R.; Ibáñez-Redín, G.; Tirich, B.; Gonçalves, D.; Balogh, D.T.; Oliveira, O.N. Fully-Printed Electrochemical Sensors Made With Flexible Screen-Printed Electrodes Modified by Roll-To-Roll Slot-Die Coating. *Biosens. Bioelectron.* **2020**, *165*, 112428. [CrossRef]
6. Bariya, M.; Shahpar, Z.; Park, H.; Sun, J.; Jung, Y.; Gao, W.; Nyein, H.Y.Y.; Liaw, T.S.; Tai, L.; Ngo, Q.P. Roll-to-roll gravure printed electrochemical sensors for wearable and medical devices. *ACS Nano* **2018**, *12*, 6978–6987. [CrossRef] [PubMed]
7. Keränen, K.; Korhonen, P.; Happonen, T.; Paakkolanvaara, M.; Kangas, J.; Rönkä, K. High throughput R2R printing, testing and assembly processing of flexible RGB LED displays. In Proceedings of the 2018 7th Electronic System-Integration Technology Conference (ESTC), Dresden, Germany, 18–21 September 2018.
8. Corletto, A.; Hosseinmardi, A.; Annamalai, P.K.; Martin, D.J.; Shapter, J.G. High-Resolution R2R-Compatible Printing of Carbon Nanotube Conductive Patterns Enabled by Cellulose Nanocrystals. *ACS Appl. Nano Mater.* **2022**, *5*, 1574–1587. [CrossRef]
9. Kooy, N.; Mohamed, K.; Pin, L.T.; Guan, O.S. A Review of Roll-To-Roll Nanoimprint Lithography. *Nanoscale Res. Lett.* **2014**, *9*, 1–13. [CrossRef]
10. Toren, P.; Rumpfer, M.; Smolka, M.; Haase, A.; Ruttloff, S.; Nees, D.; Stadlober, B.; Katzmayer, I.; Hierschlager, B.; Kierstein, S. High-throughput Roll-to-roll Production of Bio-functionalized Polymer Components. *Eur. J. Mater. Sci. Eng.* **2020**, *5*, 11–16. [CrossRef]
11. Vig, A.L.; Mäkelä, T.; Majander, P.; Lambertini, V.; Ahopelto, J.; Kristensen, A. Roll-to-roll fabricated lab-on-a-chip devices. *J. Micromech. Microengineering* **2011**, *21*, 035006. [CrossRef]
12. Habermehl, A.; Strobel, N.; Eckstein, R.; Bolse, N.; Mertens, A.; Hernandez-Sosa, G.; Eschenbaum, C.; Lemmer, U. Lab-on-chip, surface-enhanced Raman analysis by aerosol jet printing and roll-to-roll hot embossing. *Sensors* **2017**, *17*, 2401. [CrossRef] [PubMed]
13. Global SMT&Packaging Electronics Manufacturing Technologies. Available online: <https://globalsmtasia.com/flexible-electronic-devices-with-roll-to-roll-overmolding-technology/> (accessed on 10 February 2023).
14. Krebs, F.C.; Gevorgyan, S.A.; Alstrup, J. A Roll-to-roll Process to Flexible Polymer Solar Cells: Model Studies, Manufacture and Operational Stability Studies. *J. Mater. Chem.* **2009**, *19*, 5442–5451. [CrossRef]
15. Steenberg, T.; Hjuler, H.A.; Terkelsen, C.; Sánchez, M.T.; Cleemann, L.N.; Krebs, F.C. Roll-to-roll coated PBI membranes for high temperature PEM fuel cells. *Energy Environ. Sci.* **2012**, *5*, 6076–6080. [CrossRef]
16. Mauger, S.A.; Neyerlin, K.C.; Yang-Neyerlin, A.C.; More, K.L.; Ulsh, M. Gravure coating for roll-to-roll manufacturing of proton-exchange-membrane fuel cell catalyst layers. *J. Electrochem. Soc.* **2018**, *165*, F1012. [CrossRef]
17. Søndergaard, R.; Hösel, M.; Angmo, D.; Larsen-Olsen, T.T.; Krebs, F.C. Roll-to-roll fabrication of polymer solar cells. *Mater. Today* **2012**, *15*, 36–49. [CrossRef]
18. Subramanian, V.; Fréchet, J.M.; Chang, P.C.; Huang, D.C.; Lee, J.B.; Molesa, S.E.; Murphy, A.R.; Redinger, D.R.; Volkman, S.K. Progress toward development of all-printed RFID tags: Materials, processes, and devices. *Proc. IEEE* **2005**, *93*, 1330–1338. [CrossRef]
19. Wang, Y.; Huang, Y.; Li, Y.; Cheng, P.; Cheng, S.; Liang, Q.; Xu, Z.; Chen, H.; Feng, Z. A facile process combined with roll-to-roll flexographic printing and electroless deposition to fabricate RFID tag antenna on paper substrates. *Compos. Part B Eng.* **2021**, *224*, 109194. [CrossRef]
20. Dumond, J.J.; Yee Low, H. Recent developments and design challenges in continuous roller micro-and nanoimprinting. *J. Vac. Sci. Technol. B Nanotechnol. Microelectron. Mater. Process. Meas. Phenom.* **2012**, *30*, 010801. [CrossRef]
21. Ahn, S.H.; Guo, L.J. Large-area roll-to-roll and roll-to-plate nanoimprint lithography: A step toward high-throughput application of continuous nanoimprinting. *ACS Nano* **2009**, *3*, 2304–2310. [CrossRef]
22. Liedert, C.; Rannaste, L.; Kokkonen, A.; Huttunen, O.; Liedert, R.; Hiltunen, J.; Hakalahti, L. Roll-to-roll manufacturing of integrated immunodetection sensors. *ACS Sens.* **2020**, *5*, 2010–2017. [CrossRef]
23. Fung, C.M.; Lloyd, J.S.; Samavat, S.; Deganello, D.; Teng, K.S. Facile fabrication of electrochemical ZnO nanowire glucose biosensor using roll to roll printing technique. *Sens. Actuators B Chem.* **2017**, *247*, 807–813. [CrossRef]

24. Chekol, F.; Mehretie, S.; Hailu, F.A.; Tolcha, T.; Megersa, N.; Admassie, S. Roll-to-Roll printed PEDOT/PSS/GO Plastic Film for Electrochemical Determination of Carbofuran. *Electroanalysis* **2019**, *31*, 1104–1111. [[CrossRef](#)]
25. Martín, A.; Kim, J.; Kurniawan, J.F.; Sempionatto, J.R.; Moreto, J.R.; Tang, G.; Campbell, A.S.; Shin, A.; Lee, M.Y.; Liu, X. Epidermal microfluidic electrochemical detection system: Enhanced sweat sampling and metabolite detection. *ACS Sens.* **2017**, *2*, 1860–1868. [[CrossRef](#)] [[PubMed](#)]
26. Katseli, V.; Economou, A.; Kokkinos, C. Smartphone-addressable 3D-printed electrochemical ring for nonenzymatic self-monitoring of glucose in human sweat. *Anal. Chem.* **2021**, *93*, 3331–3336. [[CrossRef](#)] [[PubMed](#)]
27. Simoska, O.; Duay, J.; Stevenson, K.J. Electrochemical detection of Multianalyte biomarkers in wound healing efficacy. *ACS Sens.* **2020**, *5*, 3547–3557. [[CrossRef](#)] [[PubMed](#)]
28. Zheng, X.; Hu, Q.; Wang, Z.; Nie, W.; Wang, P.; Li, C. Roll-to-roll layer-by-layer assembly bark-shaped carbon nanotube/Ti3C2Tx MXene textiles for wearable electronics. *J. Colloid Interface Sci.* **2021**, *602*, 680–688. [[CrossRef](#)]
29. Hempel, M.; Lu, A.; Hui, F.; Kpulun, T.; Lanza, M.; Harris, G.; Palacios, T.; Kong, J. Repeated roll-to-roll transfer of two-dimensional materials by electrochemical delamination. *Nanoscale* **2018**, *10*, 5522–5531. [[CrossRef](#)]
30. Balliu, E.; Andersson, H.; Engholm, M.; Öhlund, T.; Nilsson, H.; Olin, H. Selective laser sintering of inkjet-printed silver nanoparticle inks on paper substrates to achieve highly conductive patterns. *Sci. Rep.* **2018**, *8*, 10408. [[CrossRef](#)]
31. Wolf, F.M.; Perelaer, J.; Stumpf, S.; Bollen, D.; Kriebel, F.; Schubert, U.S. Rapid low-pressure plasma sintering of inkjet-printed silver nanoparticles for RFID antennas. *J. Mater. Res.* **2013**, *28*, 1254–1261. [[CrossRef](#)]
32. Schroder, K.A.; Rawson, I.M.; Pope, D.S.; Farnsworth, S. Photonic curing explanation and application to printing copper traces on low temperature substrates. In *International Symposium on Microelectronics; International Microelectronics Assembly and Packaging Society*: San Diego, CA, USA, 2011.
33. Das, S.; Cormier, D.; Williams, S. Potential for multi-functional additive manufacturing using pulsed photonic sintering. *Procedia Manuf.* **2015**, *1*, 366–377. [[CrossRef](#)]
34. Chou, S.; Sun, B.; Fan, T.; Chiang, Y.; Chiao, J.-C.; Wu, P. Fabrication of biocompatible and conductive polypropylene micromembrane as a soft and porous electrode. *J. Taiwan Inst. Chem. Eng.* **2021**, *129*, 381–388. [[CrossRef](#)]
35. Chou, S.; Sun, B.; Cheang, W.; Tso, K.; Fan, T.; Chiao, J.-C.; Wu, P. A flexible bioelectrode based on IrO<sub>2</sub>-coated metallized polypropylene micromembrane. *Ceram. Int.* **2021**, *47*, 32554–32561. [[CrossRef](#)]
36. Chou, S.; Hsieh, Y.; Cheang, W.; Sun, B.; Chu, C.; Chen, S.; Chiao, J.-C.; Wu, P. A flexible IrO<sub>2</sub> membrane for pH sensing. *Sci. Rep.* **2022**, *12*, 11712. [[CrossRef](#)] [[PubMed](#)]
37. Dong, Q.; Sun, X.; He, S. Iridium Oxide Enabled Sensors Applications. *Catalysts* **2021**, *11*, 1164. [[CrossRef](#)]
38. Kassanos, P.; Seichepine, F.; Wales, D.; Yang, G. Towards a flexible/stretchable multiparametric sensing device for surgical and wearable applications. In *Proceedings of the IEEE Biomedical Circuits and Systems Conference (BioCAS)*, Nara, Japan, 17–19 October 2019.
39. Teymourian, H.; Tehrani, F.; Mahato, K.; Wang, J. Lab under the skin: Microneedle based wearable devices. *Adv. Healthc. Mater.* **2021**, *10*, 2002255. [[CrossRef](#)] [[PubMed](#)]
40. Huang, F.; Jin, Y.; Wen, L.; Mu, D.; Cui, M. Effects of thermal oxidation cycle numbers and hydration on IrOx pH sensor. *J. Electrochem. Soc.* **2013**, *160*, B184. [[CrossRef](#)]
41. Bahrami, H.; Mirbozorgi, S.A.; Ameli, R.; Rusch, L.A.; Gosselin, B. Flexible, polarization-diverse UWB antennas for implantable neural recording systems. *IEEE Trans. Biomed. Circuits Syst.* **2015**, *10*, 38–48. [[CrossRef](#)]
42. Shamma-Donoghue, S.A.; May, G.A.; Cotter, N.E.; White, R.L.; Simmons, F.B. Thin-film multielectrode arrays for a cochlear prosthesis. *IEEE Trans. Electron Devices* **1982**, *29*, 136–144. [[CrossRef](#)]
43. Kreider, K. Iridium Oxide Thin-Film Stability in High-temperature Corrosive Solutions. *Sens. Actuators B Chem.* **1991**, *5*, 165–169. [[CrossRef](#)]
44. Fox, G.R.; Sun, S.; Takamatsu, T. Properties of reactively sputtered IrOx for PZT electrode applications. *Integr. Ferroelectr.* **2000**, *31*, 47–56. [[CrossRef](#)]
45. Wilson, A.A.; Graziano, M.B.; Leff, A.C.; Hanrahan, B.; Baker, D.R.; Rivas, M.; Sánchez, B.; Parker, T.; Sunal, P. Growth conditions and mechanisms for IrOx nano-platelet formation by reactive sputtering. *J. Cryst. Growth* **2022**, *577*, 126374. [[CrossRef](#)]
46. Comstock, D.J.; Christensen, S.T.; Elam, J.W.; Pellin, M.J.; Hersam, M.C. Synthesis of nanoporous activated iridium oxide films by anodized aluminum oxide templated atomic layer deposition. *Electrochem. Commun.* **2010**, *12*, 1543–1546. [[CrossRef](#)]
47. Choi, W.; Papautsky, I. Fabrication of a needle-type pH sensor by selective electrodeposition. *J. Micro/Nanolithography MEMS MOEMS* **2011**, *10*, 020501. [[CrossRef](#)]
48. Rouhi, J.; Kakooei, S.; Ismail, M.C.; Karimzadeh, R.; Mahmood, M.R. Development of iridium oxide sensor for surface pH measurement of a corroding metal under deposit. *Int. J. Electrochem. Sci* **2017**, *12*, 9933–9943. [[CrossRef](#)]
49. Marsh, P.; Manjakkal, L.; Yang, X.; Huerta, M.; Le, T.; Thiel, L.; Chiao, J.; Cao, H.; Dahiya, R. Flexible iridium oxide based pH sensor integrated with inductively coupled wireless transmission system for wearable applications. *IEEE Sens. J.* **2020**, *20*, 5130–5138. [[CrossRef](#)]
50. Huang, W.; Wang, J.; Ativanichayaphong, T.; Chiao, M.; Chiao, J.-C. Development of an IrOx micro pH sensor array on flexible polymer substrate. In *Nanosensors and Microsensors for Bio-Systems*; SPIE: Vancouver, BC, Canada, 2008.
51. Yang, X.; Chiao, J.-C. In Integrated pH and Sodium Sensor Array Based on Iridium Oxide Film. In *Proceedings of the IEEE Sensors Conference*, New Delhi, India, 28–31 October 2018.

52. Zea, M.; Moya, A.; Fritsch, M.; Ramon, E.; Villa, R.; Gabriel, G. Enhanced performance stability of iridium oxide-based pH sensors fabricated on rough inkjet-printed platinum. *ACS Appl. Mater. Interfaces* **2019**, *11*, 15160–15169. [[CrossRef](#)]
53. Mariani, F.; Serafini, M.; Gualandi, I.; Arcangeli, D.; Decataldo, F.; Possanzini, L.; Tessarolo, M.; Tonelli, D.; Fraboni, B.; Scavetta, E. Advanced wound dressing for real-time pH monitoring. *ACS Sens.* **2021**, *6*, 2366–2377. [[CrossRef](#)]
54. Mahltig, B.; Textor, T. Silver containing sol-gel coatings on polyamide fabrics as antimicrobial finish-description of a technical application process for wash permanent antimicrobial effect. *Fibers Polym.* **2010**, *11*, 1152–1158. [[CrossRef](#)]
55. Vihodceva, S.; Kukle, S.; Muter, O. Antimicrobial properties of the modified cotton textiles by the sol-gel technology. In *Advanced Materials Research*; Trans Tech Publications Ltd.: Stafa-Zurich, Switzerland, 2015; Volume 1117, pp. 213–216.
56. Trovato, V.; Teblum, E.; Kostikov, Y.; Pedrana, A.; Re, V.; Nessim, G.D.; Rosace, G. Sol-gel approach to incorporate millimeter-long carbon nanotubes into fabrics for the development of electrical-conductive textiles. *Mater. Chem. Phys.* **2020**, *240*, 122218. [[CrossRef](#)]
57. Nguyen, C.M.; Huang, W.-D.; Rao, S.; Hung, C.; Tata, U.; Chiao, M.; Chiao, J.-C. Sol-Gel Iridium Oxide-Based pH Sensor Array on Flexible Polyimide Substrate. *IEEE Sens. J.* **2013**, *13*, 3857–3864. [[CrossRef](#)]
58. Huang, W.; Hsu, L.; Wang, J.; Ativanichayaphong, T.; Deb, S.; Chiao, M.; Chiao, J.-C. Investigation of repeatability of sol-gel iridium oxide pH sensor on flexible substrate. In *Micro-and Nanotechnology: Materials, Processes, Packaging, and Systems IV*; SPIE: Vancouver, BC, Canada, 2008.
59. Christianson, A.M.; Waters, C.A. Silver chloride waste recycling as a guided-inquiry experiment for the instrumental analysis laboratory. *J. Chem. Educ.* **2021**, *99*, 1014–1020. [[CrossRef](#)]
60. Kay, R.; Desmulliez, M. A review of stencil printing for microelectronic packaging. *Solder. Surf. Mt. Technol.* **2012**, *24*, 38–50. [[CrossRef](#)]
61. Phair, J.; Newton, L.; McCormac, C.; Cardosi, M.F.; Leslie, R.; Davis, J. A disposable sensor for point of care wound pH monitoring. *Analyst* **2011**, *136*, 4692–4695. [[CrossRef](#)] [[PubMed](#)]
62. Zuliani, C.; Matzeu, G.; Diamond, D. A potentiometric disposable sensor strip for measuring pH in saliva. *Electrochim. Acta* **2014**, *132*, 292–296. [[CrossRef](#)]
63. Liu, Y.; Pharr, M.; Salvatore, G.A. Lab-on-skin: A review of flexible and stretchable electronics for wearable health monitoring. *ACS Nano* **2017**, *11*, 9614–9635. [[CrossRef](#)] [[PubMed](#)]
64. Chawang, K.; Chou, S.; Bing, S.; Wu, P.; Chiao, J.-C. Porous Polypropylene Membrane Based pH Sensing for Skin Monitoring. *IEEE Access* **2022**, *10*, 111675–111687. [[CrossRef](#)]
65. Yang, X.; Chawang, K.; Chiao, J.-C. Wearable Iridium Oxide pH Sensors for Sweat pH Measurements. In Proceedings of the IEEE Sensors Conference, Montreal, QC, Canada, 28–30 October 2019.
66. Yang, X.; De Angeli, M.; Fu, J.; Dubey, S.; Chiao, J.-C. Miniature pH sensors on ultra-flexible substrates. In Proceedings of the IEEE Sensors Conference, Glasgow, UK, 29 October–1 November 2017.
67. Cao, H.; Peng, Y.; Chiao, J.-C. An integrated flexible implantable L-glutamate sensor. In Proceedings of the IEEE Sensors Conference, Waikoloa, HI, USA, 1–10 November 2010.
68. Nguyen, C.M.; Rao, S.; Yang, X.; Dubey, S.; Mays, J.; Cao, H.; Chiao, J. Sol-gel Deposition of Iridium Oxide for Biomedical Micro-devices. *Sensors* **2015**, *15*, 4212–4228. [[CrossRef](#)]
69. Jones, E.M.; Cochrane, C.A.; Percival, S.L. The effect of pH on the extracellular matrix and biofilms. *Adv. Wound Care* **2015**, *4*, 431–439. [[CrossRef](#)]
70. Shi, L.; Ramsay, S.; Ermis, R.; Carson, D. pH in the bacteria-contaminated wound and its impact on clostridium histolyticum collagenase activity: Implications for the use of collagenase wound debridement agents. *J. Wound Ostomy Cont. Nurs.* **2011**, *38*, 514–521. [[CrossRef](#)]
71. Ullah, A.; Jang, M.; Khan, H.; Choi, H.J.; An, S.; Kim, D.; Kim, Y.; Kim, U.; Kim, G.M. Microneedle array with a pH-responsive polymer coating and its application in smart drug delivery for wound healing. *Sens. Actuators B Chem.* **2021**, *345*, 130441. [[CrossRef](#)]
72. Momen-Heravi, F.; Balaj, L.; Alian, S.; Trachtenberg, A.J.; Hochberg, F.H.; Skog, J.; Kuo, W.P. Impact of biofluid viscosity on size and sedimentation efficiency of the isolated microvesicles. *Front. Physiol.* **2012**, *3*, 162. [[CrossRef](#)] [[PubMed](#)]
73. Kucukal, E.; Man, Y.; Hill, A.; Liu, S.; Bode, A.; An, R.; Kadambi, J.; Little, J.A.; Gurkan, U.A. Whole blood viscosity and red blood cell adhesion: Potential biomarkers for targeted and curative therapies in sickle cell disease. *Am. J. Hematol.* **2020**, *95*, 1246–1256. [[CrossRef](#)] [[PubMed](#)]
74. Nader, E.; Skinner, S.; Romana, M.; Fort, R.; Lemonne, N.; Guillot, N.; Gauthier, A.; Antoine-Jonville, S.; Renoux, C.; Hardy-Dessources, M. Blood rheology: Key parameters, impact on blood flow, role in sickle cell disease and effects of exercise. *Front. Physiol.* **2019**, *10*, 1329. [[CrossRef](#)]
75. Cosnahan, T.; Watt, A.A.; Assender, H.E. Flexography printing for organic thin film transistors. *Mater. Today Proc.* **2018**, *5*, 16051–16057. [[CrossRef](#)]

76. Mogg, B.T.; Claypole, T.; Deganello, D.; Phillips, C. Flexographic printing of ultra-thin semiconductor polymer layers. *Transl. Mater. Res.* **2016**, *3*, 015001. [[CrossRef](#)]
77. Huang, W.; Cao, H.; Deb, S.; Chiao, M.; Chiao, J.C. A Flexible pH Sensor Based on the Iridium Oxide Sensing Film. *Sens. Actuators A Phys.* **2011**, *169*, 1–11. [[CrossRef](#)]
78. Madeira, G.D.M.; NP Dias Mello, H.J.; Faleiros, M.C.; Mulato, M. Model improvement for super-Nernstian pH sensors: The effect of surface hydration. *J. Mater. Sci.* **2021**, *56*, 2738–2747. [[CrossRef](#)]
79. Osaka, A.; Takatsuna, T.; Miura, Y. Iridium oxide films via sol-gel processing. *J. Non Cryst. Solids* **1994**, *178*, 313–319. [[CrossRef](#)]
80. Nishio, K.; Tsuchiya, T. Electrochromic thin films prepared by sol-gel process. *Sol. Energy Mater. Sol. Cells* **2001**, *68*, 279–293. [[CrossRef](#)]
81. Chou, J.; Weng, C. Sensitivity and hysteresis effect in Al<sub>2</sub>O<sub>3</sub> gate pH-ISFET. *Mater. Chem. Phys.* **2001**, *71*, 120–124. [[CrossRef](#)]
82. Uppuluri, K.; Lazouskaya, M.; Szwagierczak, D.; Zaraska, K.; Tamm, M. Fabrication, potentiometric characterization, and application of screen-printed RuO<sub>2</sub> pH electrodes for water quality testing. *Sensors* **2021**, *21*, 5399. [[CrossRef](#)] [[PubMed](#)]
83. Xu, B.; Zhang, W. Modification of vertically aligned carbon nanotubes with RuO<sub>2</sub> for a solid-state pH sensor. *Electrochim. Acta* **2010**, *55*, 2859–2864. [[CrossRef](#)]
84. Liao, Y.; Chou, J. Preparation and characterization of the titanium dioxide thin films used for pH electrode and procaine drug sensor by sol-gel method. *Mater. Chem. Phys.* **2009**, *114*, 542–548. [[CrossRef](#)]
85. Manjakkal, L.; Cvejic, K.; Kulawik, J.; Zaraska, K.; Szwagierczak, D.; Stojanovic, G. Sensing mechanism of RuO<sub>2</sub>-SnO<sub>2</sub> thick film pH sensors studied by potentiometric method and electrochemical impedance spectroscopy. *J. Electroanal. Chem.* **2015**, *759*, 82–90. [[CrossRef](#)]
86. Olthuis, W.; Robben, M.; Bergveld, P.; Bos, M.; Van der Linden, W.E. pH Sensor Properties of Electrochemically Grown Iridium Oxide. *Sens. Actuators B Chem.* **1990**, *2*, 247–256. [[CrossRef](#)]
87. Parmar, J.S.; Shafi, N.; Sahu, C. Electrical Characterization and Study of Current Drift Phenomena and Hysteresis Mechanism in Junctionless Ion-Sensitive Field-Effect Transistor. *Silicon* **2022**, *14*, 6829–6836. [[CrossRef](#)]
88. Chawang, K.; Chou, S.; Bing, S.; Wu, P.; Chiao, J.-C. Characterization of pH Sensors Based on Iridium Oxide and Gold Encapsulated Polypropylene Membranes. In Proceedings of the IEEE Sensors Conference, Sydney, Australia, 31 October–3 November 2021.
89. Yao, S.; Wang, M.; Madou, M. A pH electrode based on melt-oxidized iridium oxide. *J. Electrochem. Soc.* **2001**, *148*, H29. [[CrossRef](#)]
90. Hendrikse, J.; Olthuis, W.; Bergveld, P. A method of reducing oxygen induced drift in iridium oxide pH sensors. *Sens. Actuators B Chem.* **1998**, *53*, 97–103. [[CrossRef](#)]
91. Burke, L.D.; Lyons, M.E.; O’Sullivan, E.; Whelan, D.P. Influence of hydrolysis on the redox behaviour of hydrous oxide films. *J. Electroanal. Chem. Interfacial Electrochem.* **1981**, *122*, 403–407. [[CrossRef](#)]
92. Papeschi, G.; Bordi, S.; Beni, C.; Ventura, L. Use of an iridium electrode for direct measurement of pI of proteins after isoelectric focusing in polyacrylamide gel. *Biochim. Biophys. Acta Protein Struct.* **1976**, *453*, 192–199. [[CrossRef](#)]
93. Karagounis, V.A.; Liu, C.C.; Neuman, M.R.; Romankiw, L.T.; Leary, P.A.; Cuomo, J.J. A Pd-PdO Film Potentiometric pH Sensor. *IEEE Trans. Biomed. Eng.* **1986**, *33*, 113–116. [[CrossRef](#)] [[PubMed](#)]
94. Turner, M.J.; Avolio, A.P. Does replacing sodium excreted in sweat attenuate the health benefits of physical activity? *Int. J. Sport Nutr. Exerc. Metab.* **2016**, *26*, 377–389. [[CrossRef](#)] [[PubMed](#)]
95. Chawang, K.; Bing, S.; Chiao, J.-C. Effects of Viscosity and Salt Interference for Planar Iridium Oxide and Silver Chloride pH Sensing Electrodes on Flexible Substrate. *Chemosensors* **2022**, *10*, 371. [[CrossRef](#)]
96. Chawang, K.; Bing, S.; Chiao, J.-C. Investigation of pH Sensing in Viscous Salt-added Solution by Iridium Oxide Film. In Proceedings of the IEEE Sensors Conference, Dallas, TX, USA, 30 October–2 November 2022.
97. Lindner, E.; Guzinski, M.; Khan, T.A.; Pendley, B.D. Reference electrodes with ionic liquid salt bridge: When will these innovative novel reference electrodes gain broad acceptance? *ACS Sens.* **2019**, *4*, 549–561. [[CrossRef](#)]
98. Dormandy, J.A. Clinical significance of blood viscosity. *Ann. R. Coll. Surg. Engl.* **1970**, *47*, 211–228.
99. Pohl, H.R.; Wheeler, J.S.; Murray, H.E. Sodium and potassium in health and disease. *Interrelat. Between Essent. Met. Ions Hum. Dis.* **2013**, *13*, 29–47.
100. Hernandez-Jaimes, C.; Lobato-Calleros, C.; Sosa, E.; Bello-Pérez, L.A.; Vernon-Carter, E.J.; Alvarez-Ramirez, J. Electrochemical Characterization of Gelatinized Starch Dispersions: Voltammetry and Electrochemical Impedance Spectroscopy on Platinum Surface. *Carbohydr. Polym.* **2015**, *124*, 8–16. [[CrossRef](#)]
101. Li, Y.; Mao, Y.; Xiao, C.; Xu, X.; Li, X. Flexible pH sensor based on a conductive PANI membrane for pH monitoring. *RSC Adv.* **2020**, *10*, 21–28. [[CrossRef](#)]
102. Yoon, J.H.; Hong, S.B.; Yun, S.; Lee, S.J.; Lee, T.J.; Lee, K.G.; Choi, B.G. High performance flexible pH sensor based on polyaniline nanopillar array electrode. *J. Colloid Interface Sci.* **2017**, *490*, 53–58. [[CrossRef](#)]
103. Possanzini, L.; Decataldo, F.; Mariani, F.; Gualandi, I.; Tessarolo, M.; Scavetta, E.; Fraboni, B. Textile sensors platform for the selective and simultaneous detection of chloride ion and pH in sweat. *Sci. Rep.* **2020**, *10*, 17180. [[CrossRef](#)]
104. Rahimi, R.; Ochoa, M.; Parupudi, T.; Zhao, X.; Yazdi, I.K.; Dokmeci, M.R.; Tamayol, A.; Khademhosseini, A.; Ziaie, B. A low-cost flexible pH sensor array for wound assessment. *Sens. Actuators B Chem.* **2016**, *229*, 609–617. [[CrossRef](#)]

105. Choi, S.; Savagatrup, S.; Kim, Y.; Lang, J.H.; Swager, T.M. Precision pH sensor based on WO<sub>3</sub> nanofiber-polymer composites and differential amplification. *ACS Sens.* **2019**, *4*, 2593–2598. [[CrossRef](#)] [[PubMed](#)]
106. Lonsdale, W.; Wajrak, M.; Alameh, K. Manufacture and application of RuO<sub>2</sub> solid-state metal-oxide pH sensor to common beverages. *Talanta* **2018**, *180*, 277–281. [[CrossRef](#)] [[PubMed](#)]

**Disclaimer/Publisher’s Note:** The statements, opinions and data contained in all publications are solely those of the individual author(s) and contributor(s) and not of MDPI and/or the editor(s). MDPI and/or the editor(s) disclaim responsibility for any injury to people or property resulting from any ideas, methods, instructions or products referred to in the content.